

CHAPTER 6

Accretion Power in Astrophysics

Daniel O. Gómez^{1,2}

(1) *Instituto de Astronomía y Física del Espacio, C.C. 67, Suc. 28,*
(1428) Buenos Aires, Argentina,

(2) *Departamento de Física, Universidad de Buenos Aires, (1428)*
Buenos Aires, Argentina, dgomez@df.uba.ar

Abstract. Accretion disks are observed in association with a variety of astrophysical objects, ranging from binary systems to active galactic nuclei. A very efficient energy conversion process is believed to take place in accretion disks, transforming gravitational energy into kinetic and thermal energy of the plasma, and typically converting them into X-ray sources. Within the general framework of hydrodynamics and magnetohydrodynamics, we present the basic features required to perform a theoretical description of the process of accretion for a number of cases of astrophysical interest.

1. Introduction

The gravitational accretion of matter is ubiquitous in Astrophysics. It is a mechanism able to efficiently convert gravitational energy into kinetic energy. This kinetic energy can in turn be converted into heat and radiation, or it can also power relativistic jets.

The advent of high resolution X-ray observations required to seek for new mechanisms to power intense X-ray sources such as binaries, quasars or Active Galactic Nuclei (AGN).

The gravitational energy delivered by one gram landing on an object of mass M and radius R is $\Delta E_{acc}/m = GM/R$. For a compact object such as a neutron star (i.e. $M \approx 1M_{\odot}$ and $R \approx 10km$) the accreted energy is

$$\frac{\Delta E_{acc}}{m} = \frac{GM}{R} \approx 10^{20} \frac{erg}{g} \quad (1)$$

For the sake of comparison, the energy per gram delivered by fusion of hydrogen is

$$\frac{\Delta E_{fus}}{m} \approx 0.007c^2 \approx 6 \cdot 10^{18} \frac{erg}{g} \quad (2)$$

If mass is continuously being accreted at a rate \dot{M} , the so called accretion luminosity is

$$L_{acc} = \frac{GM\dot{M}}{R} \quad (3)$$

For an extremely compact object such as a black hole, we use the Schwarzschild radius $R = R_{Sch} = 2GM/c^2$ and obtain that $L_{acc} \approx \dot{M}c^2$, which simply states that virtually all the accreted rest mass is absorbed by the black hole. Even though we call it *luminosity*, note that in general it is just accreted energy per unit time.

Active galactic nuclei (AGNs) have luminosities of about 10^{47} erg/s . If we have to power these objects with nuclear fusion (with its 0.7% efficiency), it will demand a very high mass rate of $\dot{M} \approx 250M_{\odot}/\text{yr}$. For a black hole instead, even at 10% efficiency, it requires only $\dot{M} \approx 20M_{\odot}/\text{yr}$.

Very luminous objects produce radiation pressure on their surrounding material, mostly through Thomson scattering so that the net radial force on every atom is

$$F_r = -\frac{GMm_p}{r^2} + \frac{\sigma_T}{c} \frac{L}{4\pi r^2} \quad (4)$$

where $\sigma_T = 6.7 \cdot 10^{-25} \text{ cm}^2$ is the cross-section for Thomson scattering.

This expression poses an upper limit to the luminosity of an object of mass M , known as Eddington's luminosity:

$$L_{Edd} = \frac{4\pi GMm_p c}{\sigma_T} \approx 1.310^{38} \frac{M}{M_{\odot}} \frac{\text{erg}}{\text{s}} \quad (5)$$

For luminosities larger than L_{Edd} , the radiation pressure exerted by photons overcomes the gravitational force, thus halting the accretion process.

Therefore, AGNs would require central objects in excess of $M \approx 10^9 M_{\odot}$ if powered by accretion. The only plausible candidates for such a high concentration of mass are supermassive black holes.

In this paper we concentrate on the basic features that allow a theoretical description of accretion disks. Many lines of research have been developed and hundreds of papers have been published in this fascinating area of Astrophysics, but a thorough description of these results is well beyond the scope of this presentation. A descriptive study of the general scenario of accretion in binary systems is given in §2. In §3 we introduce the theoretical framework of hydrodynamics, which is the approach that we use throughout the rest of the paper. The purely hydrodynamic equations (i.e. with no magnetic field) are listed in subsection 3.1., and the natural extension to include magnetic effects (i.e. magnetohydrodynamics) is given in subsection 3.2. The particular case of spherical accretion is addressed in §4, including the classical *Bondi* model (see subsection 4.2.). The theoretical description of thin disks is discussed with some detail in §5, showing the important of viscosity in the accretion process. In §6 we describe a few microphysical processes, specially those that might seriously affect the large scale dynamics of disks, such as the so called magneto-rotational instability (see subsection 6.1.). Finally, in §7 we summarize the main conclusions of this study.

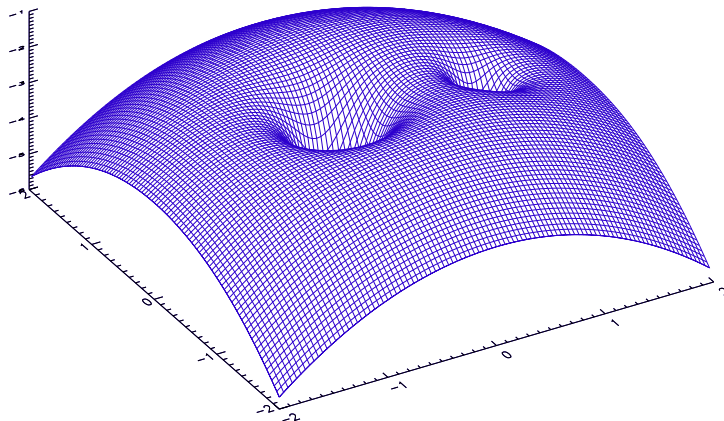


Figure 1. Roche potential for a mass ratio $q = M_2/M_1 = 1/3$.

2. Accretion in binary systems

Accretion disks can also generate in binary systems, specially in X-ray binaries. This is particularly important, since probably a fair fraction of all stars are binaries. Mass transfer in binaries can occur when one of the stars displays an intense wind, and some of this matter is gravitationally captured by its companion. Also, mass transfer in binaries can arise when one of the stars in its evolution increases its radius or when the binary separation is reduced, and fills its Roche lobe. At least in this second scenario, the mass being transferred, also carries angular momentum. Angular momentum is crucial for the formation of a disk, and it is just as important for the disk to somehow get rid of its angular momentum for the accretion mechanism to proceed. The orbital period T and separation a of a binary system with masses M_1 and M_2 are related through Kepler's law, i.e.

$$\Omega^2 = \left(\frac{2\pi}{T}\right)^2 = \frac{G(M_1 + M_2)}{a^3} \quad (6)$$

The mass flow between the stars is described from the rotating frame by

$$\frac{\partial \mathbf{u}}{\partial t} + (\mathbf{u} \cdot \nabla) \mathbf{u} = -\nabla \Phi - 2\boldsymbol{\Omega} \times \mathbf{u} - \frac{1}{\rho} \nabla p \quad (7)$$

where

$$\Phi = -\frac{GM_1}{|\mathbf{r} - \mathbf{r}_1|} - \frac{GM_2}{|\mathbf{r} - \mathbf{r}_2|} - \frac{1}{2} |\boldsymbol{\Omega} \times \mathbf{r}|^2 \quad (8)$$

is the Roche potential. The shape of the Roche potential is fully determined by the mass ratio. In Figure 1 we show the Roche potential for a mass ratio $q = M_2/M_1 = 1/3$. If for some reason we are able to neglect the Coriolis and

pressure forces (see Eqn (7)), the Roche potential provides a qualitative idea of the motion of fluid elements. The Roche lobes are the wells associated with each star, while the depletion of the potential at large distances from the binary system is a result of the centrifugal force (the last term in Eqn. (8)).

If for instance one of the stars swells up (supergiant phase) it might fill its Roche lobe and start passing matter through the L1 point, which is the local maximum between the two stars in Figure 1. The accreting star sees matter approaching from the orbiting point L1, and therefore carrying a large amount of angular momentum. Typical numbers are

$$u_{\perp} \approx 100 \frac{km}{s} \left(\frac{M}{M_{\odot}} \right)^{1/3} T_{days}^{-1/3}, \quad u_{\parallel} \approx 10 \frac{km}{s} \left(\frac{T}{10^5 K} \right)^{1/2} \quad (9)$$

Although mass would tend to describe elliptical orbits as it passes through the L1 point, dissipative processes in the flow leads to a state of minimum energy at constant angular momentum, i.e. to a circular orbit.

According to this argument, matter would form a ring rather than a disk. Also, since angular momentum does not dissipate, this ring will not be accreted. In §4 we will see that viscous torques within concentric rings will cause matter to diffuse radially, transferring mass preferentially inward and angular momentum preferentially outwards.

3. Hydrodynamic description

Hydrodynamics (HD) is a reasonable framework to describe the dynamics of gases, as long as the relevant length and time scales are respectively much larger than the mean free path and the time between collisions. When the gas particles are electrically charged, they can generate and interact with self-consistent electric and magnetic fields. The large scale dynamics of *plasmas* (i.e. electrically charged gases) is appropriately described by *magnetohydrodynamics*, as shown in Subsection 3.2.

3.1. HD equations

In the simplest cases, the state of the flow is described by the mass density $\rho(\mathbf{r}, t)$, the velocity vector field $\mathbf{u}(\mathbf{r}, t)$, and the scalar pressure $p(\mathbf{r}, t)$.

The hydrodynamic equations are, the continuity equation, which describes the conservation of mass

$$\frac{\partial \rho}{\partial t} = -\nabla \cdot (\rho \mathbf{u}), \quad (10)$$

the Navier-Stokes equation, which is the equation of motion

$$\rho \frac{\partial \mathbf{u}}{\partial t} = -\rho(\mathbf{u} \cdot \nabla) \mathbf{u} - \nabla p - \mathbf{f}_{\text{ext}} - \nabla \cdot \sigma^{\text{visc}}, \quad (11)$$

and to close the system, a polytropic equation

$$p = p_0 \left(\frac{\rho}{\rho_0} \right)^{\gamma}. \quad (12)$$

where p_0 and ρ_0 are constant reference values for pressure and mass density. For a newtonian fluid, the expression of the viscous tensor σ^{visc} (see Eqn. (11)) is

$$\sigma_{\mathbf{ij}}^{\text{visc}} = -\mu(\partial_i u_j + \partial_j u_i - \frac{2}{3}\delta_{ij}\nabla \cdot \mathbf{u}) - \xi\delta_{ij}\nabla \cdot \mathbf{u} \quad (13)$$

where μ and ξ are viscosity coefficients which depend on the thermodynamic properties of the gas.

The polytropic relation can describe physically meaningful scenarios for particular values of the parameter γ . For instance, the *adiabatic* case of monoatomic gases corresponds to $\gamma = 5/3$ and the *isothermal case* is described by $\gamma = 1$. The incompressible case is described by the limit $\gamma \rightarrow \infty$, which according to Eqn. (12) implies that changes in pressure will not be accompanied by changes in mass density. For an initially homogeneous mass distribution, the continuity equation (Eqn. (10)) in the incompressible case reduces to

$$\nabla \cdot \mathbf{u} = 0. \quad (14)$$

In more realistic cases, the polytropic equation (Eqn. (12)) is replaced by a thermodynamic equation to describe the evolution of temperature. It might include heating and cooling effects caused by viscosity, radiation and heat transfer effects such as thermal conductivity.

3.2. MHD equations

Magnetohydrodynamics is the natural extension of hydrodynamics for plasmas, i.e. gases made of electrically charged particles.

For a hydrogen plasma, fluid elements are now composed of as many electrons as protons, and therefore all fluid elements satisfy charge quasi-neutrality, i.e.

$$n(\mathbf{r}, t) = n_e = n_p \quad (15)$$

However, in general there is a net current density

$$\mathbf{j}(\mathbf{r}, t) = en_p \mathbf{u}_p - en_e \mathbf{u}_e \quad (16)$$

which is preferentially carried by the (much lighter) electrons. The current density induces magnetic fields as described by Maxwell's equations, which in turn react back on the fluid.

The electric force on each fluid element will be negligible since

$$\mathbf{f}_E = e(n_p - n_e)\mathbf{E} = 0 \quad (17)$$

while the magnetic force is

$$\mathbf{f}_B = \frac{e}{c}(n_p \mathbf{u}_p - n_e \mathbf{u}_e) \times \mathbf{B} = \frac{1}{c} \mathbf{j} \times \mathbf{B} \quad (18)$$

These equations are supplemented by Ohm's law

$$\mathbf{E}^* = \mathbf{E} + \frac{1}{c} \mathbf{u} \times \mathbf{B} = \frac{1}{\sigma} \mathbf{j} \quad (19)$$

where \mathbf{E}^* is the electric field in the reference frame of the fluid and σ is the electric conductivity of the plasma.

In summary, the Navier-Stokes equation (Eqn. (11)) for a plasma is

$$\rho \frac{\partial \mathbf{u}}{\partial t} = -\rho(\mathbf{u} \cdot \nabla) \mathbf{u} - \nabla p + \frac{1}{c} \mathbf{j} \times \mathbf{B} - \mathbf{f}_{\text{ext}} - \nabla \cdot \sigma^{\text{visc}}, \quad (20)$$

The magnetic field is generated by the plasma flow and satisfies the so called *induction equation*

$$\frac{\partial \mathbf{B}}{\partial t} = \nabla \times (\mathbf{u} \times \mathbf{B}) + \eta \nabla^2 \mathbf{B} \quad (21)$$

where $\eta = 4\pi c^2 / \sigma$ is the electric resistivity of the plasma. Equation (21) is a consequence of Ohm's law (Eqn (19)), as well as Maxwell's equations

$$\nabla \cdot \mathbf{E} = 4\pi e(n_p - n_e) \approx 0 \quad (22)$$

$$\nabla \cdot \mathbf{B} = 0 \quad (23)$$

$$\nabla \times \mathbf{E} = -\frac{1}{c} \frac{\partial \mathbf{B}}{\partial t} \quad (24)$$

$$\nabla \times \mathbf{B} = \frac{4\pi}{c} \mathbf{j} \quad (25)$$

We have neglected the displacement current in Ampere's equation (Eqn (25)), which is a reasonable assumption for non-relativistic flows, i.e. for $|\mathbf{u}| \ll c$.

4. Spherical accretion

Let us assume a spherical and stationary accretion process onto a point mass M , such that the velocity vector field points radially inward. Although the spherical and stationary assumptions constitute oversimplifications of the accretion problem, they allow a straightforward integration of the equations, which allows to gain some insight.

4.1. Spherical stationary equations

From the continuity equation (Eqn (10)) we obtain, in the stationary (i.e. $\partial_t = 0$) and spherical ($\partial_\theta = 0 = \partial_\phi$) case

$$4\pi r^2 \rho u = -\dot{M} \quad (26)$$

where the constant \dot{M} is the accretion rate. Bernoulli's theorem, arises from the stationary equation of motion when viscosity is neglected (see. Eqn (11))

$$\frac{1}{2}u^2 + \frac{\gamma}{\gamma-1} \frac{p}{\rho} - \frac{GM}{r} = \frac{\gamma}{\gamma-1} \frac{p_\infty}{\rho_\infty} \quad (27)$$

since we assume boundary values at $r \rightarrow \infty$ equal to p_∞, ρ_∞ and $u_\infty = 0$.

We define the speed of sound as $c^2 = dp/d\rho = \gamma p/\rho$. To get rid of dimensions, we use the constants $p_\infty, \rho_\infty, c_\infty$ and a typical radius $GM/(2c_\infty^2)$. The above equations in dimensionless variables become

$$\dot{m} = r^2 \rho u \quad (28)$$

$$c^2 = \rho^{\gamma-1} \quad (29)$$

$$\frac{u^2}{2} + \frac{c^2}{\gamma-1} - \frac{2}{r} = \frac{1}{\gamma-1} \quad (30)$$

We differentiate these equations with respect to the radial coordinate (the prime indicates radial derivative) and obtain

$$\frac{r}{2} \frac{u'}{u} = -\frac{c^2 - \frac{1}{r}}{c^2 - u^2} \quad (31)$$

$$\frac{r}{\gamma-1} \frac{c'}{c} = \frac{u^2 - \frac{1}{r}}{c^2 - u^2} \quad (32)$$

This set of ODE's becomes singular at every point r_* such that $u(r_*) = c(r_*)$, which are therefore called *sonic points*. This type of singularities can be avoided if we also have $u(r_*) = c(r_*) = r_*^{-1/2}$. Among the solutions of equations (31)-(32), those corresponding to accretion should satisfy that $u(r) < 0$ and $u'(r) > 0$. The existence of this kind of solutions can be assured, since the numerator and denominator in Eqn. (31) are both positive, and both simultaneously change sign at the sonic point.

4.2. Bondi model

A particularly interesting case is for the isothermal case, i.e. $\gamma = 1$, for which we have $c=1$. The first equation can be integrated to have all the possible velocity profiles:

$$\frac{u^2}{2} - \ln(ur^2) - \frac{2}{r} = E \quad (33)$$

Each solution (plotted in Figure 2) corresponds to a particular value of the integration constant E . There are only two transonic solutions, plotted in black trace. The decreasing black curve corresponds to the accretion problem (Bondi 1952). The inflowing gas reaches the sound speed at the Bondi radius

$$r_B = \frac{GM}{2c_\infty^2} \quad (34)$$

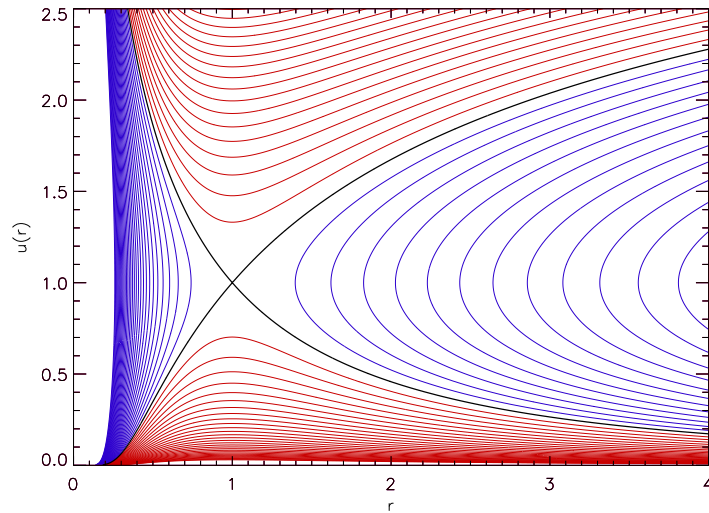


Figure 2. Radial velocity vs. radius for spherical, isothermal and stationary accretion. Black curves are separatrices. Blue curves are multivalued and considered unphysical. Red curves correspond to fully supersonic or fully subsonic solutions. The Bondi solution for accretion is the black separatrix that goes to zero at $r \rightarrow \infty$, while the Parker solution for the solar wind is the separatrix going to infinity for $r \rightarrow \infty$.

The other transonic branch, for which the velocity increases with radial distance, corresponds to Parker's wind solution (Parker 1958).

The blue solutions have to be discarded, since they are multivalued. There are two classes of red curves, those that are either fully subsonic and those fully supersonic. The subsonic solutions correspond to inefficient accretion (or wind), while the supersonic ones display unrealistic boundary conditions either at $r \rightarrow \infty$ or at $r \rightarrow 0$.

The Bondi branch corresponds to the maximum stationary accretion rate, which is

$$\dot{M} = 4\pi e^{3/2} \rho_{\infty} c_{\infty} r_B^2 \quad (35)$$

5. Thin disks

In the so called accretion disks an important energy conversion mechanism takes place, transforming gravitational energy into kinetic energy. Kinetic energy in turn transforms into heat and radiation, or it can also power intense jets. A reliable theoretical modelling of the dynamics of accretion disks is relevant for systems ranging from X-ray binaries to AGNs.

A particularly interesting theoretical problem, is the outward transport of angular momentum, as mass flows inward. This transport is controlled by the viscosity of the fluid, as shown below. In this section, we will concentrate on a hydrodynamic description of the dynamics of accretion disks.

However, magnetic fields are expected to play an important role in the dynamics of disks, in at least two very different levels. First, at a microscopic level, it seems apparent that magnetic fields cause the so called *magneto-rotational instability*. This microinstability in turn produces an enhancement of the effective viscosity of the flow, thus appreciably increasing the radial transport of angular momentum. At a macroscopic level, in many cases a fraction of the accreted mass gives rise to intense bipolar jets along the rotation axis. Although there is consensus in that magnetic fields advected by the disk are responsible for the collimation of these jets, there is still no satisfactory explanation for their formation and high degree of collimation.

One of the standard theoretical models to describe accretion is the so called *thin disk* approximation. It uses another standard model known in fluid theory as *shallow water*, which we describe in the next subsection.

5.1. Shallow water equations

We consider a disk of radius R_{disk} and half-thickness h rotating around a central object of mass M_* and radius R_* , as shown in Figure 3.

The disk is assumed to be axisymmetric (i.e. $\partial_\phi = 0$) and thin, in the sense that $h(r, t) \ll r$. We therefore use the *shallow water* approximation, which assumes that the velocity field components on the disk plane (i.e. $u_r(r, t)$ and $u_\phi(r, t)$, see Fig. 3) are independent of z , while the component u_z satisfies

$$u_z(z) = \frac{z}{h} \frac{dh}{dt} \quad (36)$$

In the incompressible limit we have $\nabla \cdot \mathbf{u} = 0$ and the mass density ρ remains constant. Combining the divergence-free condition with Equation (36), we obtain

$$\partial_t h + \frac{1}{r} \partial_r (r h u_r) = 0 \quad (37)$$

We restrict our analysis to the incompressible limit for the sake of simplicity, but the extension to compressible cases (assuming a polytropic law) is straightforward. Consistent with the shallow water approximation, we neglect the inertia terms in the \hat{z} -component of the Navier-Stokes equation, and derive the following pressure profile

$$p(r, z) = p_0 + GM\rho \left(\frac{1}{\sqrt{r^2 + z^2}} - \frac{1}{\sqrt{r^2 + h^2}} \right) \quad (38)$$

where p_0 is the external gas pressure.

In cylindrical coordinates the \hat{r} and $\hat{\phi}$ dimensionless components (using R_{disk} and $\sqrt{GM_*/R_{disk}}$ as units of longitude and velocity) of the Navier-Stokes equation are:

$$\partial_t u_\phi = -u_r \partial_r u_\phi - \frac{u_r u_\phi}{r} + \nu \left[\frac{1}{r} \partial_r (r \partial_r u_\phi) - \frac{u_\phi}{r^2} \right] \quad (39)$$

$$\partial_t u_r = -u_r \partial_r u_r + \frac{u_\phi^2}{r} + \partial_r \left(\frac{1}{\sqrt{r^2 + h^2}} \right) + \nu \left[\frac{1}{r} \partial_r (r \partial_r u_r) - \frac{u_r}{r^2} \right] \quad (40)$$

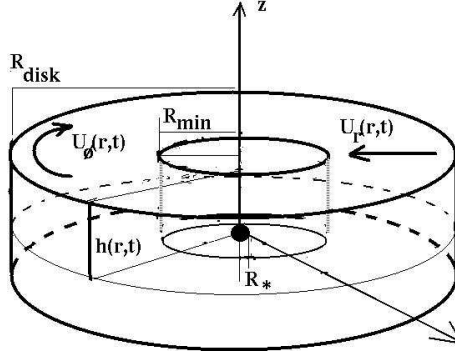


Figure 3. Cartoon of thin disk model.

where ν is the dimensionless kinematic viscosity (i.e. the inverse of the Reynolds number Re). From equations (37)-(40) we can compute the global balance of (dimensionless) quantities such as the total mass $M(t) = 2\pi \int dr rh(r,t)$

$$\partial_t M = -2\pi [rh u_r]_{R_{min}}^{R_{disk}} \quad (41)$$

angular momentum $L_z(t) = 2\pi \int dr r^2 u_\phi(r,t) h(r,t)$

$$\partial_t L_z = 2\pi \left[-hr^2 u_r u_\phi + \nu hr^3 \partial_r \left(\frac{u_\phi}{r} \right) \right]_{R_{min}}^{R_{disk}} \quad (42)$$

and mechanical energy $E(t) = 2\pi \int dr \left[\frac{u_r^2(r,t) + u_\phi^2(r,t)}{2} - \frac{1}{\sqrt{r^2 + h^2(r,t)}} \right]$

$$\partial_t E = 2\pi r h \left[-u_r \frac{u_r^2 + u_\phi^2}{2} + \frac{r^2 u_r}{(r^2 + h^2)^{3/2}} + \nu \partial_r \left(\frac{u_r^2 + u_\phi^2}{2} \right) \right]_{R_{min}}^{R_{disk}} - \nu \int_{R_{min}}^{R_{disk}} dr D \quad (43)$$

In equation (43) $D(r,t)$ is the energy dissipation function

$$D(r,t) = 2\pi h \left[r(\partial_r u_r)^2 + \frac{u_r^2}{r} + r(\partial_r u_\phi)^2 + \frac{u_\phi^2}{r} + u_\phi^2 \frac{\partial_r h}{h} \right] \quad (44)$$

Assuming that all the energy dissipated by viscous friction is converted into radiation, the disk luminosity can be simply estimated as

$$L(r,t) = \nu D(r,t) \quad (45)$$

5.2. Diffusion approximation

The equations for thin disks (i.e. $h(r,t) \ll r$) described in the previous subsection become considerably simpler if we further assume that $u_r \ll u_\phi$. In this limit, from the radial equation of motion (Eqn (40)) we obtain

$$u_\phi(r,t) \approx r^{-1/2} \quad (46)$$

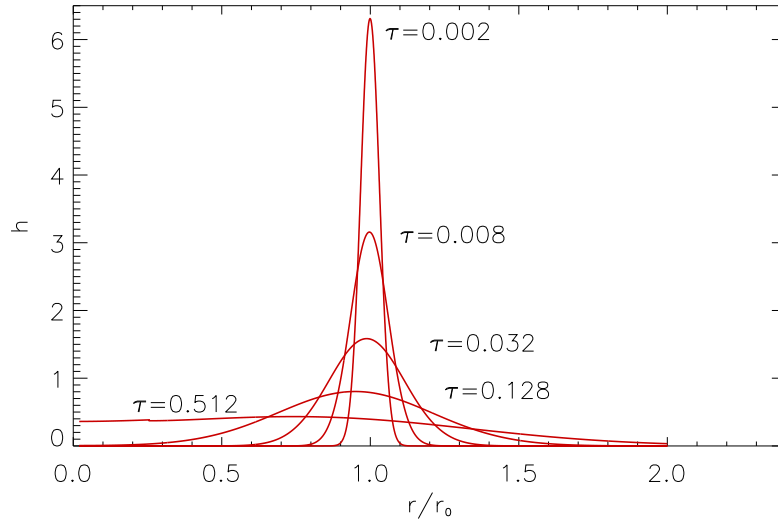


Figure 4. Disk thickness vs. radial distance for successive values of $\tau = 12\nu t/r_0^2$ (labelled).

which corresponds to a stationary Keplerian flow. Replacing this Keplerian profile into the azimuthal equation of motion (Eqn (39)), we actually obtain an expression for u_r

$$u_r(r, t) \approx -3\nu \frac{\partial_r(r^{1/2}h)}{r^{1/2}h} \quad (47)$$

As anticipated at the beginning of this section, we do not have radial fluid motion (i.e. accretion) if we do not have viscosity.

Replacing this expression for u_r into the continuity equation (Eqn (37)), we obtain

$$\frac{\partial h}{\partial t} = \frac{3\nu}{r} \partial_r \left(r^{1/2} \partial_r (r^{1/2}h) \right) \quad (48)$$

which is a diffusion equation for the disk thickness.

Let us think of a very simple scenario, consisting of a binary system with one star providing mass to the other through the L1 point, which gradually reaches a circular keplerian orbit (because dissipative processes reduce energy while conserving angular momentum) with radius r_0 . Therefore, considering as initial condition an infinitely narrow ring of radius r_0 and total mass M , i.e.

$$h(r, t = 0) = \frac{M}{2\pi\rho} \frac{\delta(r - r_0)}{r_0} \quad (49)$$

the solution of Eqn. (48) is

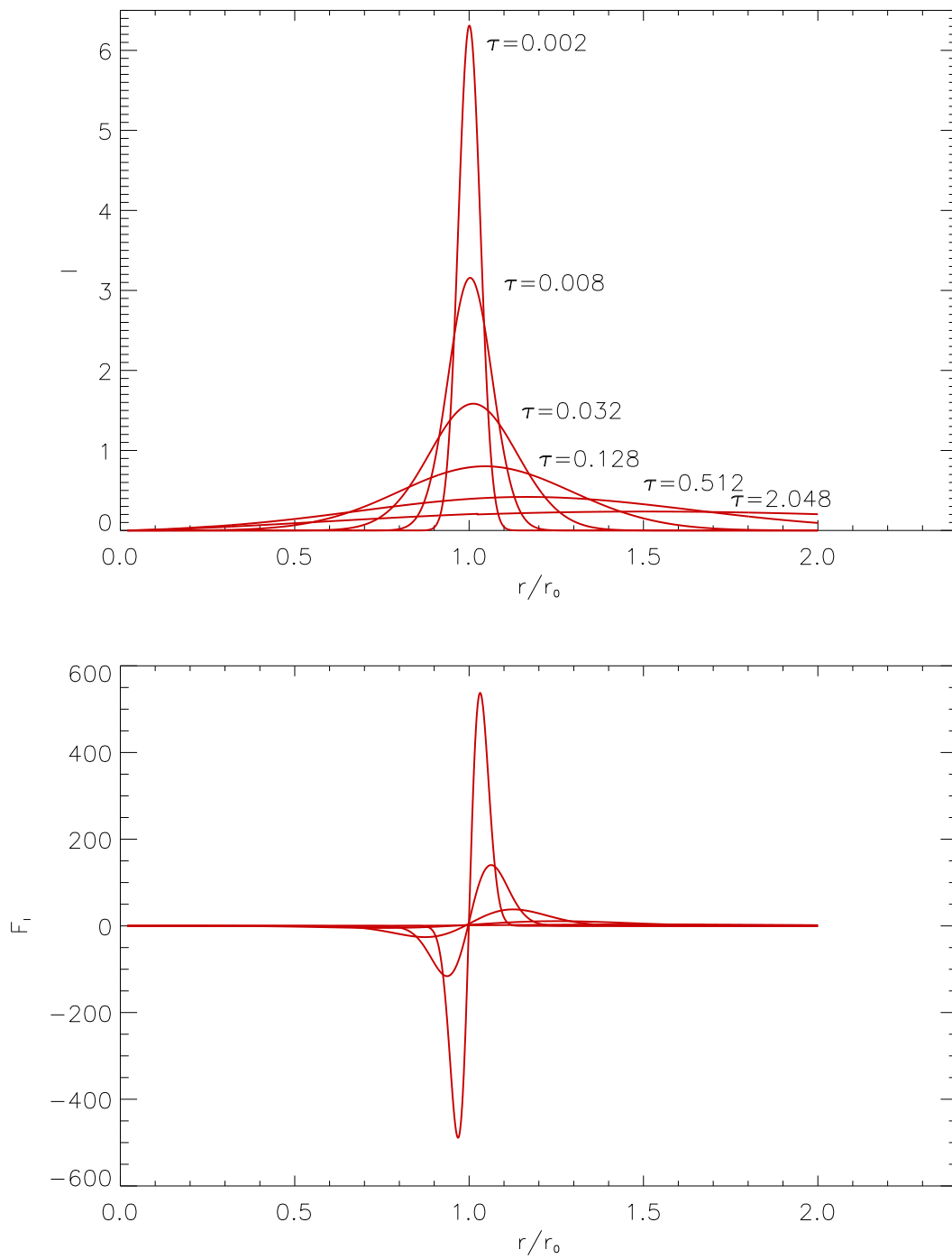


Figure 5. (a) Angular momentum density vs. radial distance for different values of τ (labelled); (b) Same as (a) for the radial flux of angular momentum.

$$h(x, \tau) = \frac{M}{\pi \rho r_0^2} \frac{e^{-\frac{1+x^2}{\tau}}}{\tau x^{1/4}} I_{1/4}\left(\frac{2x}{\tau}\right) \quad (50)$$

where $x = r/r_0$, $\tau = 12\nu t/r_0^2$ and $I_{1/4}(\cdot)$ is a modified Bessel function. This solution is displayed in Figure 4, showing different profiles $h(r)$ corresponding to different times, labelled with the value of τ . We can see that the ring is gradually shifting inwards (accretion) while at the same time it broadens in the radial direction.

In Figure 5a we show the density of angular momentum at successive times. According to the expression for angular momentum (right below Eqn (41)), the angular momentum contained in the interval $[r, r + dr]$ is $l(r, t) = 2\pi r^2 u_\phi h$. We can see in Fig. 5a that viscous diffusion causes the radial distribution of angular momentum to gradually shift outward while it also broadens. Figure 5b shows the radial flux of angular momentum at different times. From Eqn (42) we can see that the radial flux of angular momentum can be expressed as $F_l = 2\pi r h (r u_r u_\phi - \nu r^2 \partial_r (u_\phi/r))$. Fig. 5b confirms that a larger fraction of angular momentum is transported outward (i.e. $F_l > 0$), while the inner part of the ring carries a smaller part of the angular momentum inward.

5.3. Stationary models

From the stationary azimuthal equation (see Eqn (39)), we can easily obtain a first integral

$$\frac{\dot{M}}{2\pi\rho} r^2 \Omega + \nu h r^3 \Omega' = \text{const.} \quad (51)$$

which expresses the conservation of angular momentum. Using the Kepler differential rotation profile, i.e. $\Omega = u_\phi/r = r^{-3/2}$

$$\frac{\dot{M}}{2\pi\rho} - \frac{3}{2}\nu h = \frac{\text{const.}}{r^{1/2}} \quad (52)$$

The integration constant is fixed by assuming the disk thickness to vanish at a point $r = r_*$. We therefore obtain the following stationary disk profile

$$h(r) = h_\infty \left(1 - \sqrt{\frac{r_*}{r}}\right) \quad (53)$$

where $h_\infty = \dot{M}/(3\pi\rho\nu)$. Since, $-\dot{M} = 2\pi\rho h u_r$, we can also determine the radial velocity profile

Figure 6a shows the thickness profile (see also Eqn (53)) vs. radial distance, where the dotted vertical line corresponds to $r = r_*$. Figure 6b shows the velocity components vs. radial distance for a stationary regime. The blue trace corresponds to $u_r(r)$, while the red trace corresponds to $u_\phi(r)$. Note that the assumption $u_r \ll u_\phi$ breaks down sufficiently close to $r = r_*$, which calls for a more sophisticated theoretical description.

We can for instance assume $r_* \approx 0$ for a really compact object. Another usual assumption is to model the central object as a rigid rotator of radius R_*

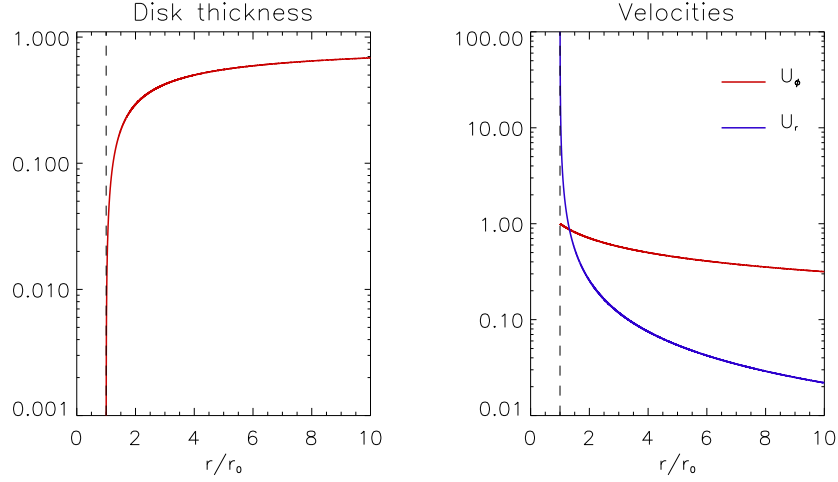


Figure 6. (a) Disk thickness vs. radial distance for a stationary regime. (b) Velocity components vs. radial distance for a stationary regime. Radial velocity $u_r(r)$ is indicated in blue, while the azimuthal velocity $u_\phi(r)$ is shown in red.

and angular velocity Ω_* . In this case the Kepler rotation profile needs to be adapted to match $\Omega(r = R_*) = \Omega_*$. This condition will generate a boundary layer of thickness δr , such that $\Omega'(R_* + \delta r) = 0$. In the asymptotic limit $\delta r \ll R_*$ we reobtain the previous profiles for $r_* = R_*$.

The energy balance equation for the portion of disk contained between R_1 and R_2 can be written as

$$\frac{dE}{dt} = -\Delta F_E - \nu D_E \quad (54)$$

where the energy is

$$E = 2\pi\rho \int_{R_1}^{R_2} dr r h \left(\frac{u_r^2 + u_\phi^2}{2} - \frac{1}{\sqrt{r^2 + h^2}} \right) \quad (55)$$

The radial energy flux F_E is

$$F_E(r) = 2\pi\rho r h \left(u_r \left(\frac{u_r^2 + u_\phi^2}{2} \right) - \frac{r^2 u_r}{(r^2 + h^2)^{3/2}} - \nu \partial_r \left(\frac{u_r^2 + u_\phi^2}{2} \right) \right) \quad (56)$$

and $\Delta F_E = F_E(R_2) - F_E(R_1)$. The energy dissipation rate D_E in this portion of disk is

$$D_E = 2\pi\rho \int_{R_1}^{R_2} dr h \left(r \partial_r (u_r)^2 + r \partial_r (u_\phi)^2 + \frac{u_r^2 + u_\phi^2}{r} + u_\phi^2 \frac{\partial_r h}{h} \right) \quad (57)$$

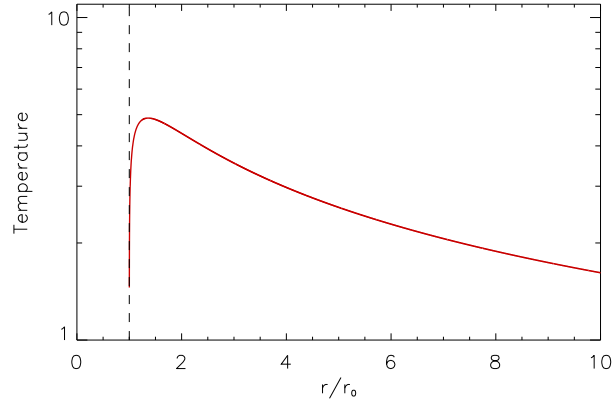


Figure 7. Temperature profile vs. radial distance for a stationary regime.

With the approximations $h \ll r$ and $u_r \ll u_\phi$, the energy dissipation rate per unit disk area $\Gamma(r)$ reduces to

$$2\pi r dr \Gamma(r) \approx 2\pi dr \rho \nu h (r\Omega')^2 \quad (58)$$

Replacing the thickness profile given in Eqn (53), we readily obtain

$$\Gamma(r) = \frac{3GM\dot{M}}{4\pi r^3} \left(1 - \sqrt{\frac{R_*}{r}}\right) \quad (59)$$

The total energy dissipated in the disk is then

$$L_{disk} = 2\pi \int_{R_*}^{\infty} dr r \Gamma(r) = \frac{1}{2} L_{acc} \quad (60)$$

where L_{acc} is the accretion luminosity (see Eqn (3)). According to this result, only half of the gravitational energy (per unit time) being accreted is actually dissipated in the disk. The other half can either dissipate in the narrow boundary layer surrounding the solid object, or can be swallowed by the central object, or else it can power intense jets.

To compute the emitted spectrum, let us assume the disk to be optically thick, even though it is geometrically thin. As a result, energy dissipated per unit area produces a blackbody flux on each face, i.e. $\sigma T^4 = \Gamma/2$. Therefore

$$T(r) = \left(\frac{3GM\dot{M}}{8\pi\sigma r^3} \left(1 - \sqrt{\frac{R_*}{r}}\right) \right)^{1/4} \quad (61)$$

According to this result, temperature reaches a maximum value at $T_{max} = 0.29(GM\dot{M}/\sigma R_*^3)^{1/4}$ at $r = 1.36R_*$, falling off at larger distances like $T \approx r^{-3/4}$ as shown in Figure 7. For typical values of white dwarf stars, is $T_{max} \approx 5 \cdot 10^4 K$, which corresponds to UV emission. On the other hand, if the compact object

is a neutron star, the maximum temperature can be as high as $T_{max} \approx 10^7 K$, which is therefore an X-ray source.

A very important observable feature that can be derived from this very simple theoretical model, is the spectrum emitted by the disk. The emitted spectrum at radial distance r can be very crudely approximated by a blackbody function, i.e.

$$I_\nu = B_\nu[T(r)] = \frac{2h\nu^3}{c^2} \frac{1}{e^{\frac{h\nu}{kT(r)}} - 1} \quad (62)$$

Since the accretion disk is not spatially resolved, to obtain the total emitted flux, we integrate Equation (62) in space. The emitted photon energy flux to be measured at a distance D from the source is

$$F_\nu = \frac{2\pi}{D^2} \int_{R_*}^{R_{out}} dr r I_\nu = \frac{4\pi h\nu^3}{c^2 D^2} \int_{R_*}^{R_{out}} dr \frac{r}{e^{\frac{h\nu}{kT(r)}} - 1} \quad (63)$$

which is shown in Figure (8) for disks of different ratios R_{out}/R_* . Note that the emitted spectrum is independent of the fluid viscosity, which is a direct consequence of having assumed a stationary regime.

Note that the *log-log* plot has the shape of a blackbody spectrum, stretched in its central part and displaying a power-law behavior like

$$F_\nu \approx \nu^{1/3} \quad (64)$$

which is considered characteristic of disks. At sufficiently small frequencies, i.e. for $h\nu \ll kT_{out}$, the spectrum can be approximated by the Jeans limit and therefore

$$F_\nu \approx \nu^2 \quad (65)$$

On the other end, at large frequencies such that $h\nu \gg kT_{out}$, the spectrum is well approximated by the Wien limit, which corresponds to an exponentially decreasing behavior.

5.4. Dynamic solutions

We developed a Fortran code to integrate the dynamic equations in the thin disk approximation (see Eqs. (37)-(40)). We used a centered finite differences scheme for the spatial derivatives and Runge-Kutta for the time integration (see Vigh et al. 2005 for further details). For the inner boundary at R_* we adopted open boundary conditions, so that any fluctuation of the variables can escape freely through that boundary. To perform relaxation simulations, we adopted open boundary conditions in the outer boundary R_{out} as well. We also performed externally driven simulations to allow for the injection of mass, angular momentum and mechanical energy at $r = R_{out}$.

To check the quality of the code, we numerically computed the various terms participating in equations (41)-(43), which describe the balance of global quantities such as mass, angular momentum and mechanical energy. In Figure 9 we display a comparison between the left hand side of each of these balance

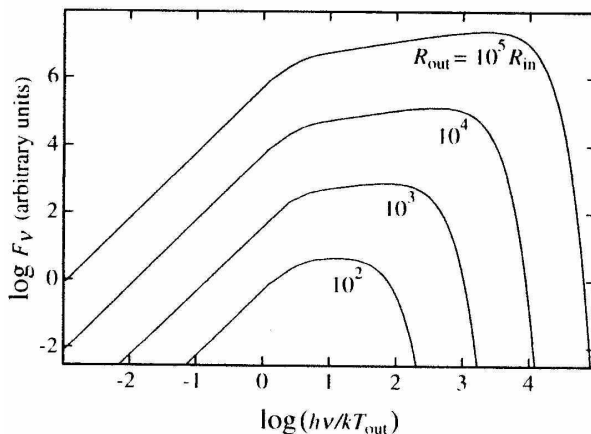


Figure 8. Emitted spectra of optically thick and geometrically thin accretion disks, for different values of the ratio R_{out}/R_* (labelled). Adapted from Frank et al. 1985.

equations vs. time (dotted line) and the right hand side (full line). The left panel corresponds to mass (i.e. equation (41)), the central panel displays the balance of angular momentum (equation (42)), and the right panel corresponds to mechanical energy (i.e. equation (43)). This particular simulation was performed with a mass injection rate $\dot{M} = 5 \cdot 10^{-5}$, a time step $\Delta t = 10^{-4}$, dimensionless viscosity $\nu = 2 \cdot 10^{-4}$, and $R_{out}/R_* = 10$.

To study the diffusion of mass, angular momentum and mechanical energy, we performed simulations starting with a relatively narrow ring of mass rotating with a Keplerian profile (i.e. $u_\phi = r^{-1/2}$). The thickness of the ring has a Gaussian radial profile and the radial velocity is initially zero. In Figure 10 we display the disk thickness vs. radius at various times throughout the simulation (left), the angular momentum density (middle) and also the expected luminosity (right),

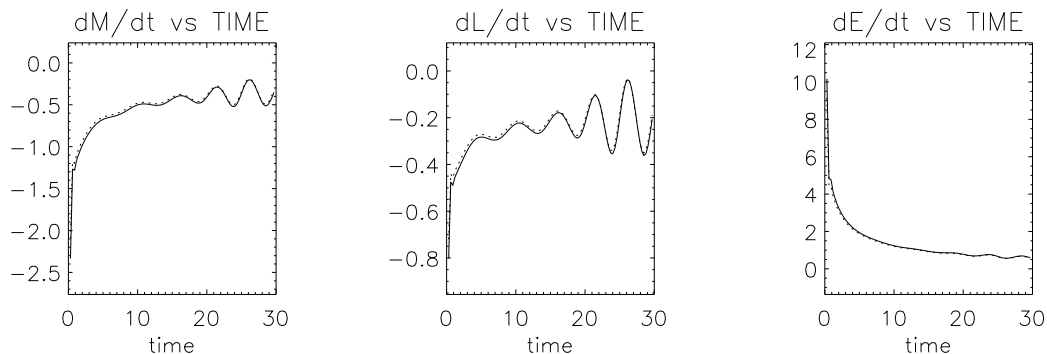


Figure 9. Balance of mass (left), angular momentum (center) and mechanical energy (right) in arbitrary units.

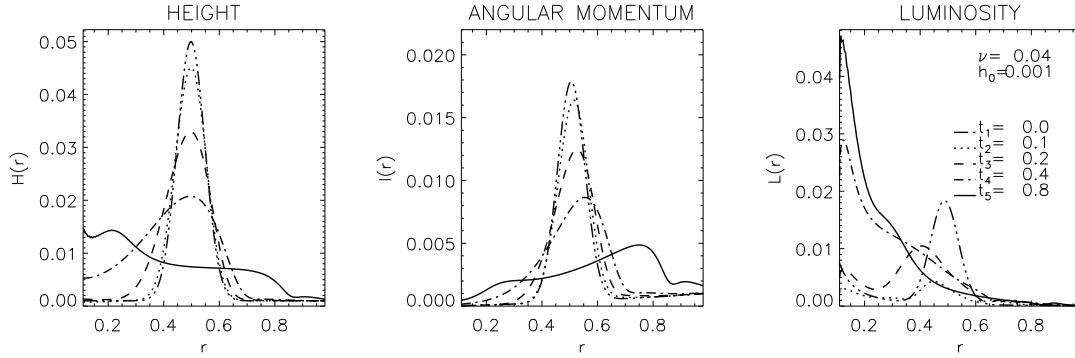


Figure 10. An initial ring of matter diffuses radially for $\nu = 0.04$. *Left:* disk thickness. *Center:* Angular momentum density. *Right:* Luminosity density.

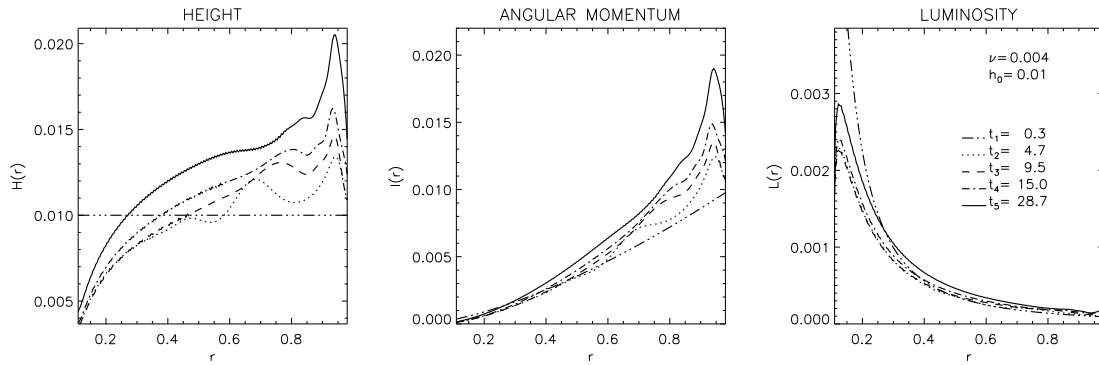


Figure 11. Externally driven run with $\nu = 4 \cdot 10^{-3}$ and $\dot{M} = 1.5 \cdot 10^{-4}$.

(right). For this particular simulation, viscosity is $\nu = 0.04$ and the boundary conditions are free in both R_* and R_{out} . We can see that while the mass distribution shifts inwards (accretion), the angular momentum diffuses outwards.

To evaluate the long-term dynamics of thin accretion disks, we performed simulations with given values of the dynamic variables in the outer boundary: $h(R_{out})$, $u_r(R_{out})$ and $u_\phi(R_{out})$. These boundary conditions translate into stationary injection of mass, angular momentum and mechanical energy. Figure 11 shows disk thickness, angular momentum and luminosity as a function of radius for various times. The propagation of gravity surface waves can be observed in this simulation, as shown in Figure 12. We speculate that gravity waves might play a role in the redistribution of angular momentum in accretion disks. Another feature which emerges rather clearly in all the externally driven simulations that we performed, is the relation toward a Keplerian rotation profile, i.e. $u_\phi = r^{-1/2}$.

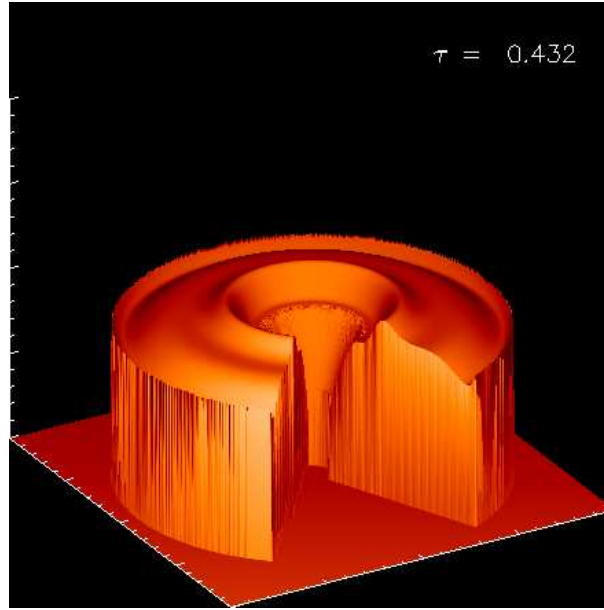


Figure 12. Image of an externally driven disk displaying the propagation of surface gravity waves.

6. Microphysics

In the previous sections we concentrated on the large scale dynamics of accretion disks. We have seen that the fluid viscosity plays a crucial role in the accretion process, as well as in the outward transport of angular momentum. Viscosity arises from the molecular diffusion that transports momentum between layers of flow. Spitzer's coefficient is therefore of the order of

$$\nu_{mol} \approx \lambda_{mfp} u_{th} \quad (66)$$

where λ_{mfp} is the mean free path of the molecules and u_{th} is their thermal speed. A crude estimate of ν_{mol} shows that it is far too small to be relevant in accretion disks. Assuming a purely HD scenario, Shakura & Sunyaev (1973) proposed that the relevant viscous stress component is simply proportional to pressure, i.e.

$$\sigma_{r\phi}^{visc} = \rho \nu_{eff} r \Omega' \approx \alpha p \quad (67)$$

where α is a dimensionless number. For an isothermal fluid is $p = \rho c_s^2$ and we now that the rotation profile is approximately keplerian, i.e. $|r\Omega'| = 3\Omega/2 \approx \Omega$. Therefore, the effective viscosity becomes

$$\nu_{eff} = \alpha \frac{c_s^2}{\Omega} = \alpha \frac{h}{c_s} \quad (68)$$

since $h/r = c_s/(r\Omega) \ll 1$ for thin disks.

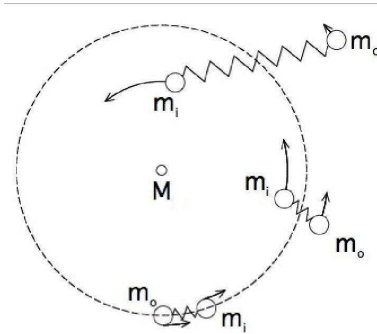


Figure 13. Cartoon model of MRI, consisting of two fluid elements advected with the differential rotation flow while undergoing an elastic interaction exerted by the magnetic field.

Equation (68) is the Shakura and Sunyaev prescription (Shakura & Sunyaev 1973), which is simply a consequence of a dimensional analysis. Our lack of knowledge on the dissipation mechanism is now hidden in the dimensionless parameter α . The physical interpretation might be that the radial speed of momentum-carrying fluctuations can not exceed the sound speed, and that the typical size of these fluctuations is the disk thickness h .

6.1. Magneto-rotational instability

Although it is still being debated, there does not seem to be purely HD instabilities able to generate microturbulence. However, the possibility of enhancing viscosity within the framework of hydrodynamics, can not be ruled out (see for instance Umurham & Regev 2004 or Lesur & Longaretti 2005). The promising candidate seems to be the magneto-rotational instability (MRI, see Velikhov 1959; Chandrasekhar 1960; also Balbus & Hawley 1991).

A simple explanation for MRI is as follows. Because of the differential rotation, two fluid elements with a small radial separation will separate further away. However, if they are threaded by a magnetic field line, the role of the magnetic force can be imitated by a spring. The effect of the spring interaction is to slow down the inner ball m_i (and reduce its angular momentum) and accelerate the outer one m_o (increasing its angular momentum). This will cause the inner ball to fall further in, and the outer one to move radially out, as sketched in Figure 13.

The mathematical version for this instability consists in perturbing the circular orbit of two particles in a central potential and adding a spring between them. The equilibrium is

$$-\Omega_0^2 r_0 = - \left(\frac{d\Phi}{dr} \right)_{r_0} \quad (69)$$

where $i\Phi(r) = \Phi_0(r/r_0)^{2(1-a)}$ and $\Omega(r) = \Omega_0(r/r_0)^{-a}$. Let us linearly perturb the equilibrium shown in Eqn (69), i.e. $r = r_0 + \delta r$ and $\phi = \Omega_0 t + \delta\phi$. To simulate the restoring force of the magnetic field we assume $\delta\mathbf{F} = -\kappa\delta\mathbf{r}$. The

equations of motion for the displacement are

$$\delta\ddot{r} - 2\Omega_0 r_0 \delta\dot{\phi} = 2a\Omega_0^2 \delta r - \kappa \delta r \quad (70)$$

$$r_0 \delta\ddot{\phi} + 2\Omega_0 \delta\dot{r} = -\kappa r_0 \delta\phi \quad (71)$$

Assuming $\delta r, \delta\phi \approx e^{-i\omega t}$ leads to the following dispersion relation

$$\omega^4 - 2\omega^2 \left(\kappa + (2-a)\Omega_0^2 \right) + \kappa(\kappa - 2a\Omega_0^2) = 0 \quad (72)$$

Let us explore two different asymptotic limits for this general expression. In the purely HD case, we do not have the spring ($\kappa = 0$) and therefore

$$\omega^2 = 2(2-a)\Omega_0^2 \quad (73)$$

which is the so called *epicyclic frequency*, and describes stable oscillations of a fluid element about its keplerian orbit.

The second asymptotic limit that we would like to address, corresponds to a non-rotating disk, i.e. $\Omega_0 = 0$. In this particular case,

$$\omega^2 = \kappa^2 = (\mathbf{k} \cdot \mathbf{v}_A)^2 \quad (74)$$

since the evolution should correspond to the propagation of Alfvén waves along the magnetic field ($\mathbf{v}_A = \mathbf{B}_0 / \sqrt{4\pi\rho}$ is the Alfvén velocity).

In summary, if we only have rotation or magnetic field, there is no instability. However, if we consider the two effects combined, replacing Eqn (74) into Eqn (72) leads to

$$\omega^2 = p + \frac{1}{2} \pm \sqrt{\left(p + \frac{1}{2}\right)^2 - p(p-3)} \quad (75)$$

where $p = (\mathbf{k} \cdot \mathbf{v}_A / \Omega_0)^2$. The two solutions of Eqn (75) are shown in Figure (14). One of the branches is stable for all values of the parameter p , but the other one shows instability for $p < 2a$. Therefore, the instability condition can be expressed as

$$|\mathbf{k} \cdot \mathbf{v}_A| < \sqrt{2a}\Omega_0 \quad (76)$$

indicating that for the instability to occur, the magnetic field has to be non-zero but at the same time needs to be sufficiently weak.

6.2. Shearing box simulations

Although global numerical simulations of the dynamics of accretion disks are currently being performed (see for instance Hawley et al. 2001), they are rather prohibitive, since one lacks the spatial resolution to simulate microscale processes. To compensate for this, one normally uses artificially enhanced viscosity coefficients.

On the other hand, for local simulations (i.e. for a small fluid parcel) it is essential to use proper boundary conditions. At least for MRI, the shear flow

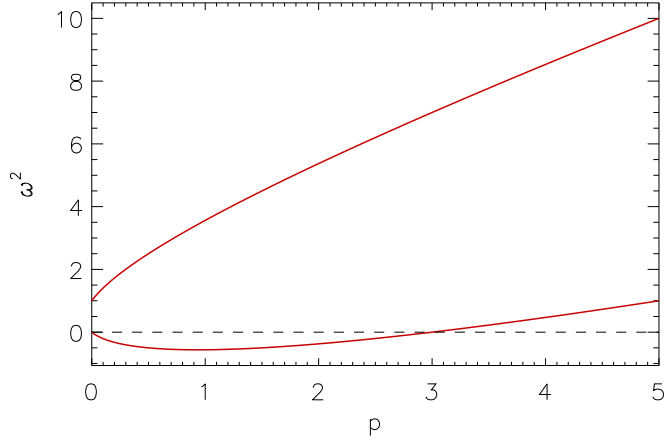


Figure 14. Dispersion relation of Eqn (74). The unstable case corresponds to $\omega^2 < 0$.

corresponding to differential rotation (i.e. for $a \neq 0$) is a central ingredient in driving the instability. The idea of *shearing boxes* was developed (see Hawley et al. 1995 and references therein) to consistently include the role of differential rotation. Locally, cartesian coordinates are used such that $(r, \phi, z) \rightarrow (x, y, z)$, with boundary conditions

$$f(x, y, z) = f(x + L_x, y - a\Omega_0 L_x t, z) , \quad (77)$$

$$f(x, y, z) = f(x, y + L_y, z) , \quad (78)$$

$$f(x, y, z) = f(x, y, z + L_z) , \quad (79)$$

for every physical quantity f , which corresponds to a box gradually shearing in the x -direction (i.e. the radial direction).

The HD equations (the extension to MHD is straightforward) in cartesian coordinates including the effect of differential rotation are

$$\frac{D\mathbf{u}}{Dt} = -\frac{1}{\rho}\nabla P - \nabla\Phi - 2\Omega_0 \times \mathbf{u} + a\Omega_0 u_x \hat{\mathbf{y}} \quad (80)$$

where the time derivate is defined as

$$\frac{D}{Dt} = \frac{\partial}{\partial t} - a\Omega_0 x \frac{\partial}{\partial y} + (\mathbf{u} \cdot \nabla) \quad (81)$$

and

$$\frac{P}{\rho} = \frac{p}{\rho} - \frac{1}{2} \|\Omega_0 \times \mathbf{r}\|^2 \quad (82)$$

As shown in Eqs. (80)-(82), the inertial forces are also considered. The Coriolis force is explicitly written (see Eqn (80)), while the centrifugal potential

has been added to the pressure term (Eqn (82)). Hawley et al. 1995 integrated these equations numerically, using a finite difference scheme to confirm the development of the MRI instability. More recently, these equations have also been numerically integrated using spectral schemes, which are much more accurate (Umurhan & Regev 2004; Lesur & Longaretti 2007).

7. Conclusions

- During this set of lectures, we tried to focus on the basic features of the dynamics of accretion disks required to perform their theoretical modelling. As a result, many of the new and exciting results on this field might not have not been fully addressed.
- We have seen the relevance of angular momentum in the accretion disk, both in providing the disk shape and their negative role in the accretion of matter.
- We have seen the requirement for microscopic processes to provide enhanced viscosity. One of the promising candidates is MRI.
- We have seen that shearing box simulations are interesting tools to study the ongoing microphysics in small fluid parcels.
- Large scale simulations do self-consistently show the development of MRI and the corresponding enhancement in the accretion process.
- One of the big questions that still remains unsolved, is the powering of the intense jets observed in association with microquasars and AGNs.

Acknowledgments. I would like to thank Drs. Gustavo Romero and Paula Benaglia as well as the rest of the organizers of the *First La Plata International School on Astronomy and Geophysics* for hosting such an outstanding meeting here in Argentina.

References

- Balbus, S.A., & Hawley, J.F. 1991, ApJ, 376, 214.
Balbus, S.A., & Hawley, J.F. 1998, Rev. Mod. Phys., 70, 1.
Biskamp, D. 1993, "Nonlinear Magnetohydrodynamics", Cambridge Univ. Press.
Bondi, H. 1952, MNRAS, 112, 195.
Chandrasekhar, S. 1960, Proc. Nat. Acad. Science USA, 46, 253.
Frank, J., King, A., & Raine, D. 1985, "Accretion power in Astrophysics", Cambridge University Press.
Hawley, J.F., Gammie, C.F., & Stone, J.M. 1995, ApJ, 440, 742.
Hawley, J.F., Balbus, S.A., & Stone, J.M. 2001, ApJ 554, L49.
Lesur, G., & Longaretti, P.Y. 2005, Astron. & Ap., 444, 25.

Parker, E.N. 1958, *ApJ*, 128, 664.

Pringle, J.E. 1981, *Ann. Rev. Astron. & Ap.*, 19, 137.

Shakura, N.I., & Sunyaev, R.A. 1973, *Astron. & Ap.*, 24, 337.

Umurhan, O.M., & Regev, O. 2004, *Astron. & Ap.*, 427, 855.

Velikhov, E.P. 1959, *Sov. Phys. JETP* 9, 995.

Vigh, C.D., Montero, M.F., & Gómez, D.O. 2005, *Bol. AAA*, 48, 352.